

Article

Investigation of Collision Toughness and Energy Distribution for Hot Press Forming Center Pillar Applied with Combination Techniques of Patchwork and Partial Softening Using Side Crash Simulation

Min Sik Lee ¹, Chul Kyu Jin ^{2,*}, Junho Suh ¹, Taekyung Lee ¹ and Ok Dong Lim ³

¹ School of Mechanical Engineering, Pusan National University, 2 Busandaehak-ro 63beon-gil, Geumjeong-gu, Busan 46241, Korea

² School of Mechanical Engineering, Kyungnam University, 7 Kyungnamdaehak-ro, Masanhappo-gu, Changwon-si 51767, Korea

³ Autogen Co., Ltd., 249, Sihwa Venture-ro, Siheung-si 15118, Korea

* Correspondence: cool3243@kyungnam.ac.kr; Tel.: +82-55-249-2346

Abstract: Various techniques can be applied to center pillars to enhance collision characteristics during side crashes. For instance, patchwork (PW) can be welded to the center pillar to increase its stiffness, and partial softening (PS) can be applied to provide ductility. Side crash tests are conducted by the Insurance Institute for Highway Safety (IIHS) to evaluate collision resistance. However, it is difficult to evaluate collision toughness and energy distribution flow for each automobile component. In this study, a side crash simulation was performed with IIHS instruction. We investigated the effect of hot press forming (HPF) a center pillar with a combination of PW and PS techniques on collision toughness and energy distribution flow. As a result, the role of PW and PS techniques were verified during side crashes. PW improved the strain energy and intrusion displacement by 10% and 7.5%, respectively, and PS improved the plastic deformation energy and intrusion displacement by 10%. When PW and PS were applied to the HPF center pillar simultaneously, a synergistic effect was achieved.

Keywords: center pillar; side crash simulation; patchwork; partial softening; energy distribution



Citation: Lee, M.S.; Jin, C.K.; Suh, J.; Lee, T.; Lim, O.D. Investigation of Collision Toughness and Energy Distribution for Hot Press Forming Center Pillar Applied with Combination Techniques of Patchwork and Partial Softening Using Side Crash Simulation. *Metals* **2022**, *12*, 1941. <https://doi.org/10.3390/met12111941>

Academic Editors: Yao Shen and Ning Gao

Received: 14 October 2022

Accepted: 7 November 2022

Published: 12 November 2022

Publisher's Note: MDPI stays neutral with regard to jurisdictional claims in published maps and institutional affiliations.



Copyright: © 2022 by the authors. Licensee MDPI, Basel, Switzerland. This article is an open access article distributed under the terms and conditions of the Creative Commons Attribution (CC BY) license (<https://creativecommons.org/licenses/by/4.0/>).

1. Introduction

In light of global environmental concerns, the automobile industry has become increasingly interested in fuel efficiency and weight reduction. With increasing demand for technological development to achieve high performance and high fuel efficiency, research on the application of advanced high-strength steel (AHSS) for automobile components has progressed [1–4].

The HPF process was introduced to enhance the stiffness and strength of automobile components. In the HPF process, a blank is heated to a high temperature to create an austenitic phase and then cooled rapidly in forming dies to form a martensite phase [5,6].

However, the use of hot stamped parts is restricted in automobile components and requiring collision absorption, owing to their low elongation. For example, in the case of a side crash, the B-pillar, also known as the center pillar, is among the most important automobile components with respect to passenger safety. During side crash impact, the center pillar must be ductile to absorb the collision energy and stiff to improve intrusion resistance. Much research has been conducted on center pillars made with alternative materials [7–9] or post tempering processes to obtain tailored properties [10,11].

Owing to productivity demands and manufacturing costs, the PW and PS techniques are well-known and widely used in the automobile industry to improve the collision characteristics of center pillars.

To improve intrusion resistance and increase the stiffness of automobile components, a PW is attached to the center pillar to achieve reinforced structural stiffness. The formability of laser-welded PW blanks was investigated by Mori et al. and Shi et al. [12,13]. The spot weld conditions to attach PW to HPF parts was optimized by Ahmad et al. [14]. Chengxi et al. studied methods to improve the mechanical properties of B-pillars with PW and predict the temperature distribution using FE simulation [15].

PS can be applied to improve energy absorption and increase the ductility of automobile components. Gao et al. investigated the characteristics of temperature-dependent IHTC of 22MnB5 during the spray-quenching process [16]. Ota et al. [17] evaluated the damage value and tailored temperature using a forming limit diagram. Bok et al. performed a simulation to predict the microstructure and mechanical properties of a B-pillar in comparison with experimental results [18]. Kim et al. manufactured a B-pillar using the partial strengthening method with minimal shape change [19]. However, the above studies investigated only the manufacturing process and were limited in that they did not evaluate the impact toughness and energy distribution flow, which affect performance when applied to an actual vehicle. A few studies have been conducted involving impact tests to evaluate the effects of PW and PS on impact toughness and energy distribution. Recently, M. S. Lee et al. manufactured an HPF center pillar with PW and PS by controlling the cooling rate and conducted experimental and numerical drop weight tests [20]. Owing to the limitations of the experimental equipment, the results were limited in terms of evaluating the energy absorption characteristics of PW and PS, and test collisions could not be conducted at high speed or using real vehicles owing to high costs.

In this study, given the importance of the evaluation of safety in high-speed collisions, a vehicle and an impactor were modeled according to the IIHS guidelines to evaluate the collision absorption capacity at high speed based on a previously verified low-speed drop weight test, as well as energy distribution in a high-speed collision. To improve stiffness and ductility, PW and PS techniques were applied to the HPF center pillar, and experiments were performed for comparison with the simulations to verify the results.

2. Experiment and Simulation

2.1. Materials

Figure 1a shows that the function of the center pillar during a side crash. Generally, the HPF center pillar has a low elongation of less than 5%, so collision toughness is not satisfied. In addition, the stiffness of the center pillar in the top region is not sufficient against intrusion resistance. The PS technique provides ductility to the HPF center pillar and, PW strengthens the stiffness of the HPF center pillar to improve collision characteristics, such as energy absorption and intrusion resistance.

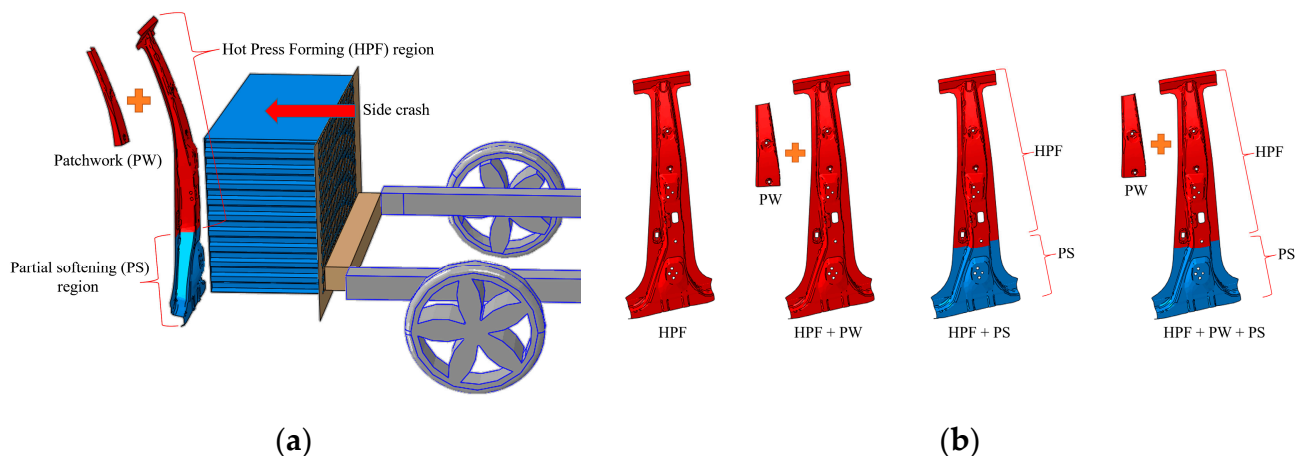


Figure 1. (a) Function of the center pillar during a side crash. (b) Four kinds center pillars [20].

In this study, a 22MnB5 boron steel sheet was used for the HPF center pillar and PW. The PS region was controlled by a cartridge heater during manufacturing of the HPF center pillar [20]. Table 1 shows the material properties of 22MnB5 (HPF) and 22MnB5 (PS). The thicknesses of the HPF center pillar and PW were both 1.2 mm. To evaluate the effect of PW and PS on energy distribution and intrusion resistance, a side crash simulation was performed with four kinds of the center pillar, as shown in Figure 1b.

Table 1. Material properties of 22MnB5 (HPF) and 22MnB5 (PS) [20].

Material	Tensile Strength (MPa)	Elongation (%)	Elastic Modulus (GPa)	Vickers Hardness (HV)
22MnB5 (HPF)	1500	5	210	440
22MnB5 (PS)	715	11~13	210	225

2.2. Drop Weight Test and Simulation

2.2.1. Geometry Modeling, Mesh, and Weld Constraints for FE Simulation

An FE simulation for the drop weight test was performed using ABAQUS/explicit software. Figure 2 shows the geometry modeling and welding constraints between the HPF center pillar and PW. The fine mesh was defined in the impact region, and the rough mesh was defined in other regions to reduce computation time. The element types of the center pillar and weld nodes were S4 and CNN3D2, respectively. The PW was welded to the HPF center pillar with $1200 \times 440 \times 51.5 \text{ mm}^3$ dimension. As shown in Figure 2b, the master weld node was defined on the element of center pillar, and the slave weld node was defined on the element of the PW. The master and slave weld nodes were bonded, and the attachment method used for the welding connector was point to point. The damage criterion and damage evolution of weld constraints were not applied because a fracture did not occur at the weld point. The detailed weld conditions for the FE simulation are listed in Table 2.

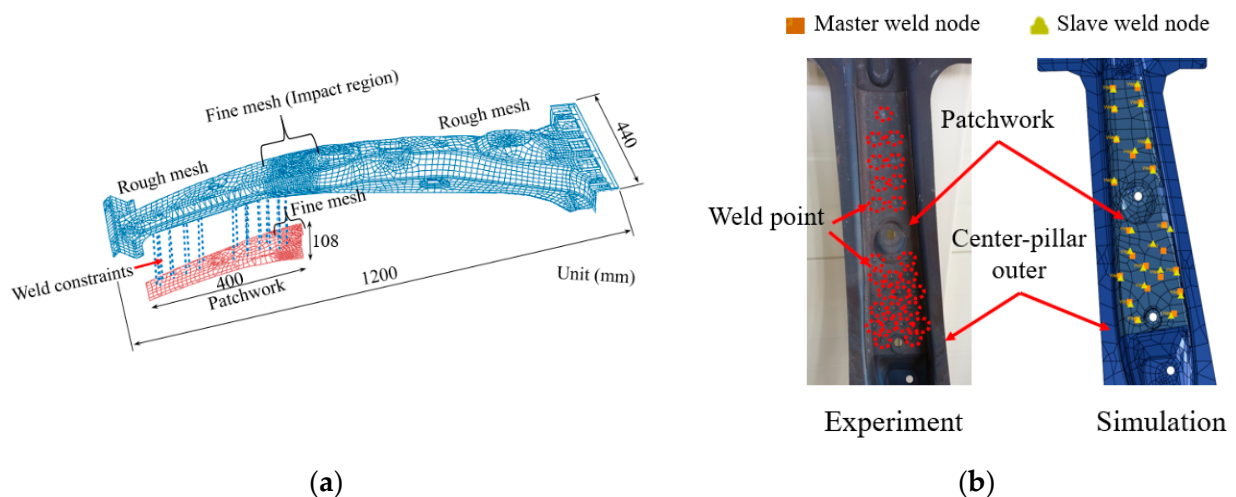


Figure 2. Center pillar and PW: (a) geometry and mesh; (b) weld constraints.

Table 2. Spot weld conditions for FE simulation.

Attachment Method	Additional Mass (kg)	Spot Radius (mm)	Degrees of Freedom
Point-to-point	0	3	0

2.2.2. Boundary Conditions for Drop Weight Test

Figure 3 shows the simulation and experimental apparatus for the drop weight test. The center pillar was fixed by clamp, as shown in Figure 3a. The drop height from the center pillar was 610 mm, and the load cell was attached to an impactor with a weight of 160 kg.

A drop weight simulation was also performed for comparison with the experimental data. The impactor velocity was 3.450 m/s before collision. The 6 degrees of freedom of the center pillar were fixed in the zig region by a clamp. The friction coefficient between the center pillar and impactor was 0.1. The collision time was 0.18 s. The detailed boundary conditions for the drop weight test are listed in Table 3.

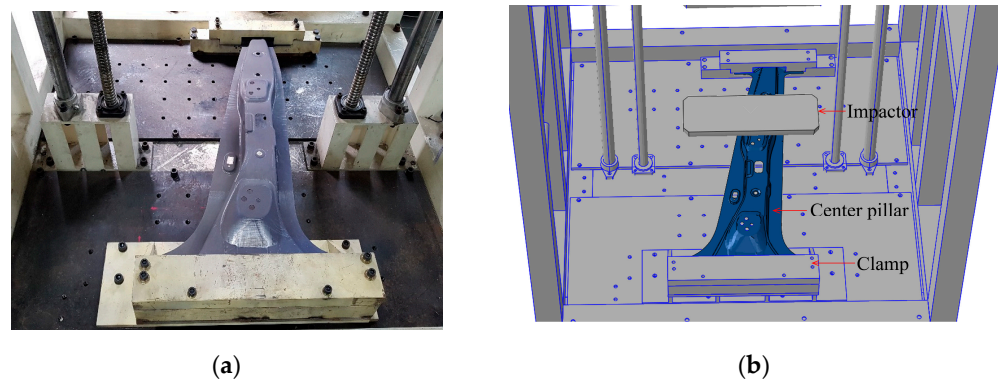


Figure 3. Boundary conditions for the drop weight test: (a) experiment; (b) simulation.

Table 3. Boundary conditions of the simulation for the drop weight test.

Impactor Mass (kg)	Collision Time (s)	Impactor Velocity (m/s)	Drop Height (mm)	Initial Potential Energy (J)	Friction Coefficient between Front Bumper Beam and Impactor
160	0.18	3.45	610	956	0.1

2.3. Side Crash Simulation

2.3.1. Geometry and Properties of a Moving Deformable Barrier in a Sedan

A moving deformable barrier (MDB) was modeled for side crash simulation according to IIHS guidelines. Figure 4 shows the geometric modeling of an MDB with dimensions of $450 \times 1000 \times 650 \text{ mm}^3$. The MDB consists of two parts: a main honeycomb block and an aluminum sheet used as the cover layer. The two parts were adhesively bonded together. The main honeycomb block was hexagonal in shape with a cell size of 22 mm made Al5052 foil. The foil thickness was 0.05 mm, with a crush strength of 31 MPa [21]. The weight of the MDB was $1360 \text{ kg} \pm 5 \text{ kg}$ with a deformable element, and the center of mass was 1000 mm from the front of the deformable element, as shown in Figure 4. The MDB roll (I_x), pitch (I_y), and yaw (I_z) moments of inertia were $542 \text{ kg}\cdot\text{m}^2$, $2471 \text{ kg}\cdot\text{m}^2$, and $2757 \text{ kg}\cdot\text{m}^2$, respectively.

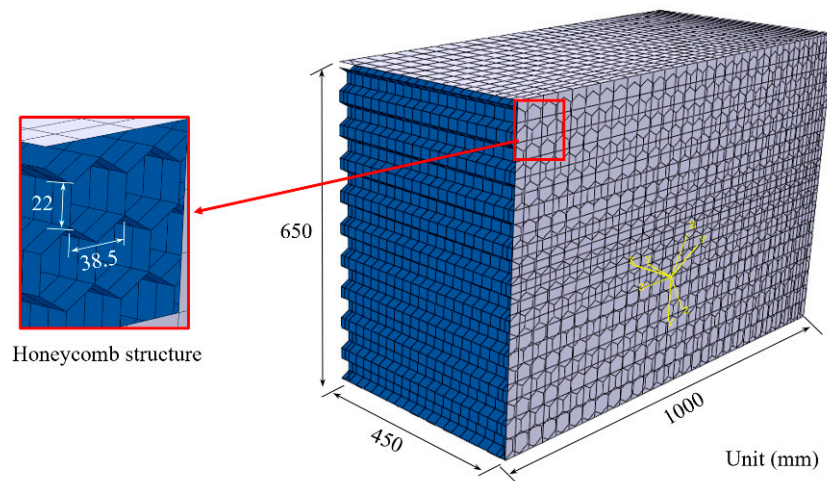


Figure 4. Geometric modeling of an MDB for side crash simulation.

Figure 5 shows the geometric modeling and material section of the automobile and pillars. The automobile geometry for used for simulation had the same dimensions as an automobile: $4580 \times 1820 \times 1250 \text{ mm}^3$. As an actual automobile, the shell model was used, and the element type was set to S4 to reduce the hourglass effect and enable detailed measurement of absorbed energy. Owing to the complexity of the shape of the automobile, with curves and had many holes, the automobile part was meshed using a bottom-up mesh technique. The collision region was finely meshed, whereas regions away from the collision area were roughly meshed. The thicknesses of the center pillar, outer and inner reinforcement, and doors and other frames were 1.2 mm, 1.2 mm, and 2.0 mm, respectively. Multiple materials were used to design the sedan. The center pillar, PW, and frame and other parts were made with HPF with PS, HPF, and DP590 and CR420 (mild steel), respectively.

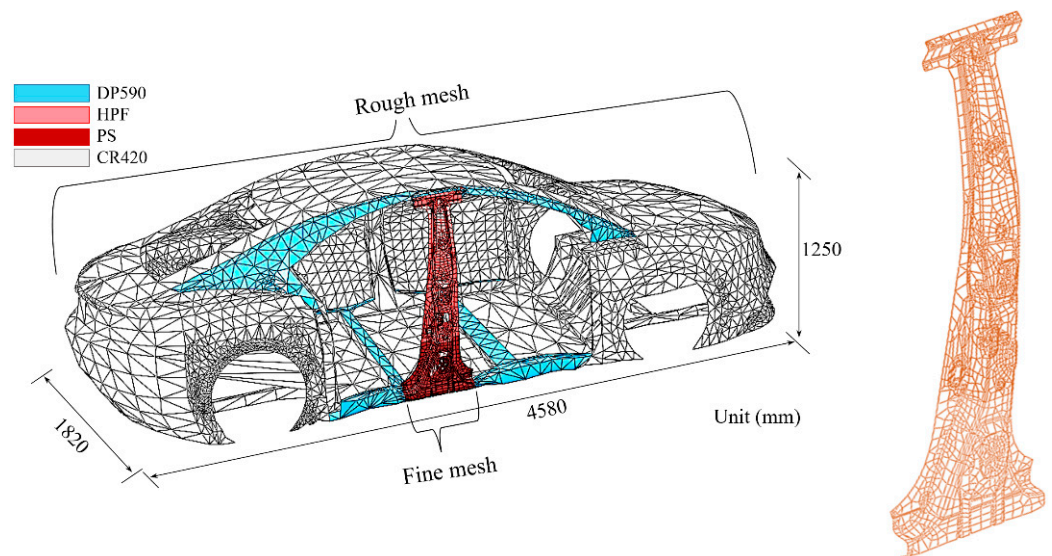


Figure 5. Geometry and material sections of the sedan for side crash test.

2.3.2. Boundary Conditions for Side Crash Test

Figure 6 shows a schematic diagram of the side crash test. A side crash test involves a stationary vehicle, evaluating the impact characteristics when an impactor equipped with an MDB collides with the side region of a stopped vehicle according to IIHS regulation. An impactor with an MDB has a collision velocity of 50 km/h (13.8 m/s) and hits the stopped vehicle at a 90 degree angle, as shown in Figure 6. The mass of the sedan and the impactor with an MDB were 1420 and 1360 kg, respectively. The 6 degrees of freedom of the stopped vehicle were fixed on the ground. The friction coefficient between the ground and the impactor's wheel was 0.1. The collision time was 0.1 s. Because the opposite side of the collision zone would not be deformed, a half body of a stopped vehicle (sedan) was used as a rigid body in order to reduce the analysis time. The detailed side crash conditions are listed in Table 4. Mass scaling was not used, and the stable time increment size was 1.67821×10^{-8} s.

Table 4. Collision conditions for side crash simulation.

Sedan Mass (kg)	MDB Mass (kg)	Collision Time (s)	Impactor Velocity (m/s)	Initial Kinetic Energy (kJ)	Friction Coefficient between Ground and Vehicle
1420	1500	0.1	13.8	142	0.1

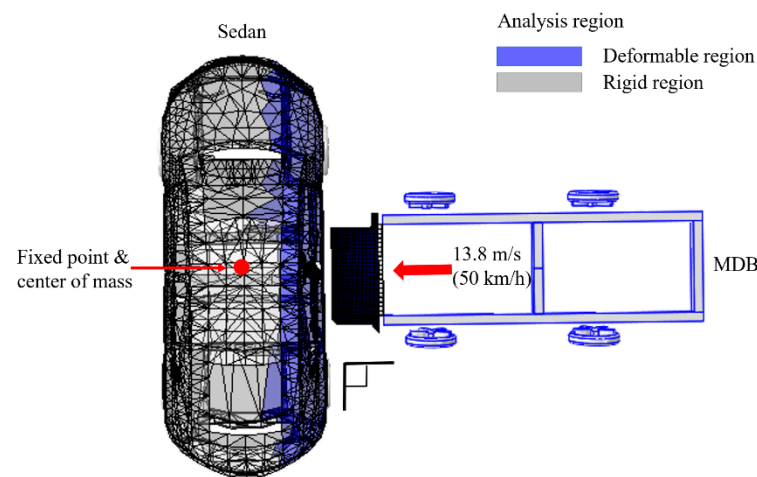


Figure 6. Boundary conditions for side crash simulation.

2.3.3. Energy Absorption Method

In the side crash simulation, the various energies, such as elastic, plastic, kinetic, friction, and viscoelastic energy, were transformed by deformation during the collision. The energy absorbed by deformation was experimentally calculated using load-displacement data according to Equation (1) [22].

$$E_{ab} = \int_0^s F(x)dx \quad (1)$$

where E_{ab} , s , and F are absorbed energy, crash displacement, and impulsive force, respectively.

The specific energy absorption (SEA) was obtained by Equation (2):

$$SEA = \frac{E_a}{M} \quad (2)$$

where M and E_a are total mass and absorbed energy, respectively.

When the SEA value is high, the energy absorption capability is high. However, this is approximate (rather than exact) estimation method and cannot determine elastic and plastic deformation energy.

In this study, the integrated stress–strain curve data per unit element volume were used to calculate the accurate absorbed energy, such as elastic and plastic dissipated energies, and for analysis of the distribution of energy flow in the time domain.

Figure 7a shows the meshed shell with the S4 element type used to accurately calculate the energy variable data and avoid the hourglass effect. As shown in Figure 7a, the shell element has 4 points, which are inside the mid-surface, in contrast with a solid element type. Because the mid-surface was used for analysis, the change in shell thickness was not visually expressed, and the strain in the thickness direction of the shell element was calculated as Equation (3):

$$\epsilon_{33} = \frac{\nu}{1-\nu}(\epsilon_{11} + \epsilon_{22}) \quad (3)$$

Treating these as logarithmic strains,

$$\ln \frac{t}{t_0} = -\frac{\nu}{1-\nu} \ln \left(\frac{l_0}{l} \right) = -\frac{\nu}{1-\nu} \ln \left(\frac{A}{A_0} \right) \quad (4)$$

where l , t , ν , and A are the element length, thickness, Poisson's ratio, and area of the shell's reference surface, respectively.

The change in shell thickness is expressed by Equation (5).

$$\frac{t}{t_0} = \left(\frac{A}{A_0}\right)^{\left(-\frac{\nu}{1-\nu}\right)} \tag{5}$$

According to the above equations, the element volume of each mesh can be measured by Equation (6) after deformation.

$$V_{element} = At_0 \left(\frac{A}{A_0}\right)^{\left(-\frac{\nu}{1-\nu}\right)} \tag{6}$$

The stress–strain curve describing the calculation of absorbed energy per element volume during deformation is shown in Figure 7b.

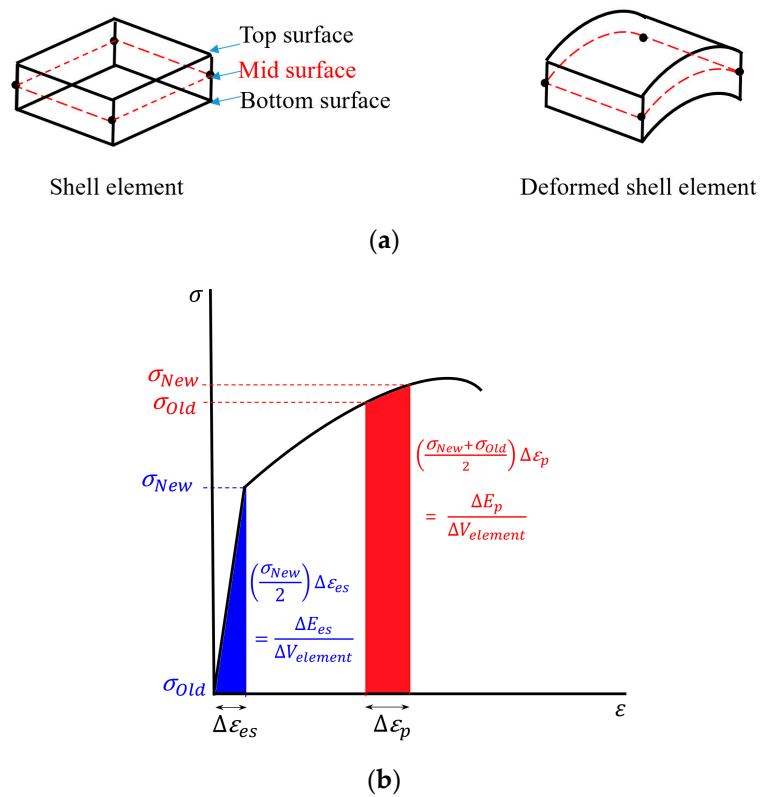


Figure 7. Shell element and energy absorption of the stress–strain curve per element volume: (a) element deformation; (b) elastic strain energy and plastic deformation energy.

As shown in Figure 7b, the specific elastic and plastic deformation energies are measured by Equations (7) and (8), respectively:

$$\Delta E_{es} = \frac{1}{2} \sigma_{New} \Delta\epsilon_{es} \Delta V \tag{7}$$

$$\Delta E_p = \frac{1}{2} (\sigma_{Old} + \sigma_{New}) \Delta\epsilon_p \Delta V \tag{8}$$

where σ_{New} , σ_{Old} , σ_u , and ΔV are the new stress, previous stress, user-defined equation stress, and specific element volume, respectively.

The internal energy can be expressed by integrating Equation (9):

$$E_I = \int_0^t \left(\int_V \sigma^u : \dot{\epsilon} dV \right) dt \tag{9}$$

Then, $\dot{\varepsilon} = \dot{\varepsilon}^{es} + \dot{\varepsilon}^p + \dot{\varepsilon}^c$ and E_I can be separated as in Equation (10):

$$E_I = \int_0^t \left(\int_V \sigma^u : \dot{\varepsilon} dV \right) dt = \int_0^t \left(\int_V \sigma^u : \dot{\varepsilon}^{es} dV \right) dt + \int_0^t \left(\int_V \sigma^u : \dot{\varepsilon}^p dV \right) dt + \int_0^t \left(\int_V \sigma^u : \dot{\varepsilon}^c dV \right) dt = E_{es} + E_p + E_c \quad (10)$$

where $\dot{\varepsilon}^{es}$, $\dot{\varepsilon}^p$, and $\dot{\varepsilon}^c$ are the elastic strain rate, plastic strain rate, and creep strain rate, respectively; and E_{es} , E_p , and E_c are the elastic energy, plastic energy, and creep strain energy, respectively.

The elastic strain energy (E_{es}) results from linear deformation, whereas energy is dissipated by plasticity (E_p) when permanent deformation of the meshed element begins. The elastic and plastic strain regions are linear and non-linear, respectively. The aforementioned energies are defined by Equations (11) and (12), respectively:

$$E_{es} = \int_0^t \left(\int_V \sigma^u : \dot{\varepsilon}^{es} dV \right) dt = \sum_t \sum_{i=1}^n \frac{1}{2} \sigma_i \varepsilon_i \Delta V_i \quad (11)$$

$$E_p = \int_0^t \left(\int_V \sigma^u : \dot{\varepsilon}^p dV \right) dt \quad (12)$$

In this study, the element set of PW, PS, and MDB was selected, as shown in Figure 8. The E_{es} and E_p of the four kinds of center pillars were compared during a side crash because the elastic strain and plastic deformation energies account for most of the internal energy, which is known as the absorbed energy during a collision. E_{es} and E_p of PS and PW were calculated using the above equation during the deformation of the element according to the four types of center pillars, as shown in Figure 1b.

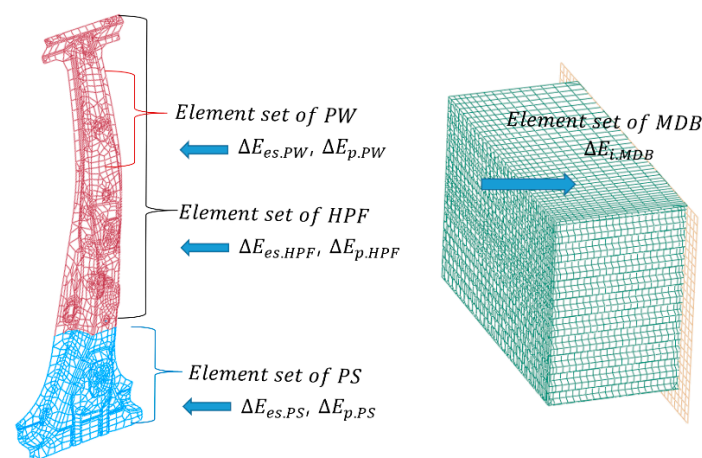


Figure 8. Energy distribution of the center pillar and MDB.

2.3.4. Damage Initiation Criteria and Damage Evolution

Local necking in the shell element could not be realized because the sheet metal in the simulation was very thin. To predict the onset of necking instability, the forming limit diagram (FLD) curve was used in this study. Simulations were performed by applying the previously obtained FLD for 22MnB5 (HPF and PS) to Abaqus/explicit [23,24].

3. Results and Discussion

3.1. Comparison of Impulse between Experiment and Simulation

Figure 9 compares the experimental and simulation results after the collision test for the HPF center pillar with PW and PS. Figure 9a,b show the top and side views of the center pillar, respectively, between the experiment and the simulation. The figure shows that the deformation behaviors of the experiment and the simulation were similar [20].

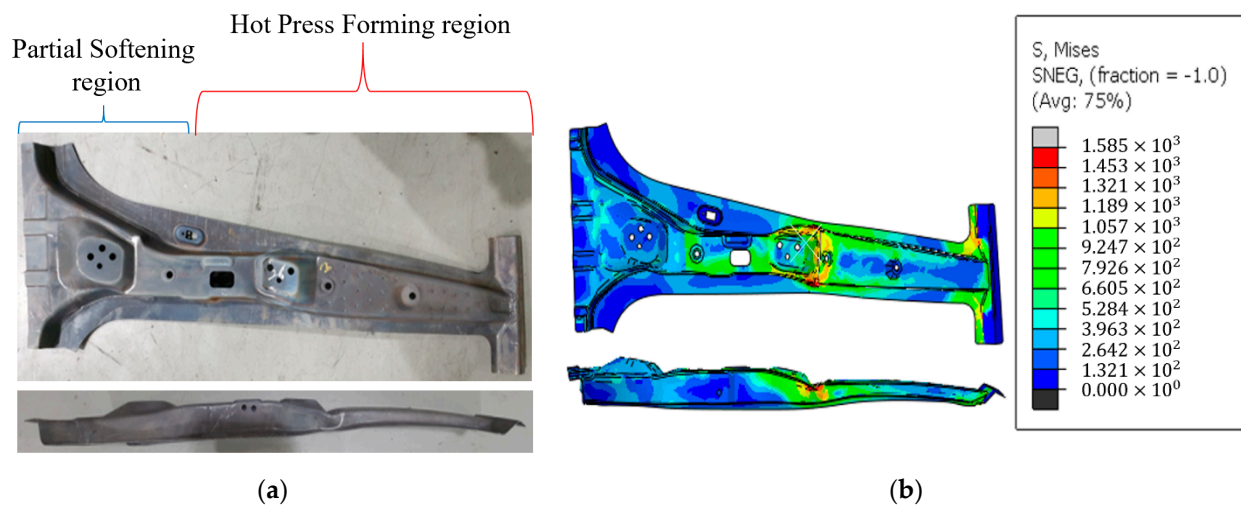


Figure 9. Comparison of the HPF center pillar with PW and PS after the drop weight test: (a) top and side view after the experiment; (b) top and side view after the simulation [20].

Figure 10 shows the comparison result of impactor load between experiment and simulation according to time. The maximum impact load of the experiment and simulation were 9.5 kN and 12.7 kN, respectively. The value of impulse and collision time between the experiment and simulation were 799 N·s, 0.165 s and 787 N·s, 0.117 s, respectively. Based on above results, the simulation and experiment were validated, and these material sections of mechanical properties were used for side crash simulation.

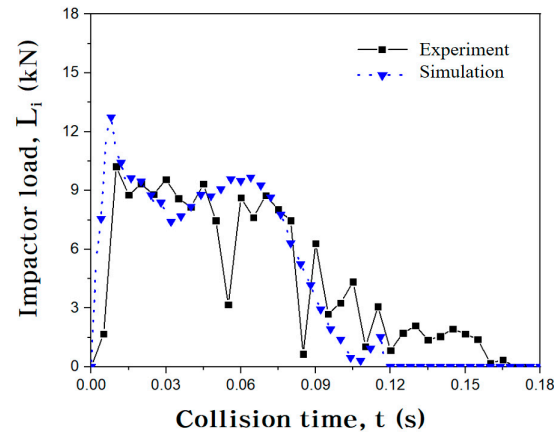


Figure 10. Comparison of the impactor load of the HPF center pillar with PW between the experiment and the simulation [20].

3.2. Side Crash Simulation

3.2.1. Energy Distribution during Side Crash Simulation

The first law of thermodynamics is the law of conservation of energy. In an isolated system, the total energy remains constant, even when the energy changes from one form to another. The energy can be converted into various types in an automobile side impact, such as kinetic energy, potential energy, internal energy, or friction dissipation energy. In general, most kinetic energy in an automobile crash causes a considerable change in internal energy as a result of elastic and plastic deformation. Total energy can be measured as the sum of several energies according to Equation (13):

$$E_{total} = E_i + E_k + E_v + E_f + E_e \quad (13)$$

where E_i , E_k , E_v , E_f , and E_e are internal energy, kinetic energy, viscous dissipation energy, friction dissipation energy, and external work, respectively.

Figure 11 shows the distribution of the total energy during the side crash. The total energy is 142 kJ. First, the velocity of MDB decreased gradually as a result of friction between the ground and MDB before the collision. The E_k decreased sharply during the collision because the velocity of the MDB decreased, whereas the E_i was increased by plastic and elastic deformation, and E_v increased to 5.8 kJ as a result of material damping. During the collision, other energies increased, but total energies were maintained. For example, when the collision time was 0.0385 s, the E_{i-MDB} , $E_{i-Sedan}$, E_k , E_v , and E_f were 45.1 kJ, 45.7 kJ, 45.4 kJ, 2.9 kJ, and 5.9 kJ, respectively, as shown in Figure 11a,b. The value of E_e was 0 kJ because the external work had not yet occurred.

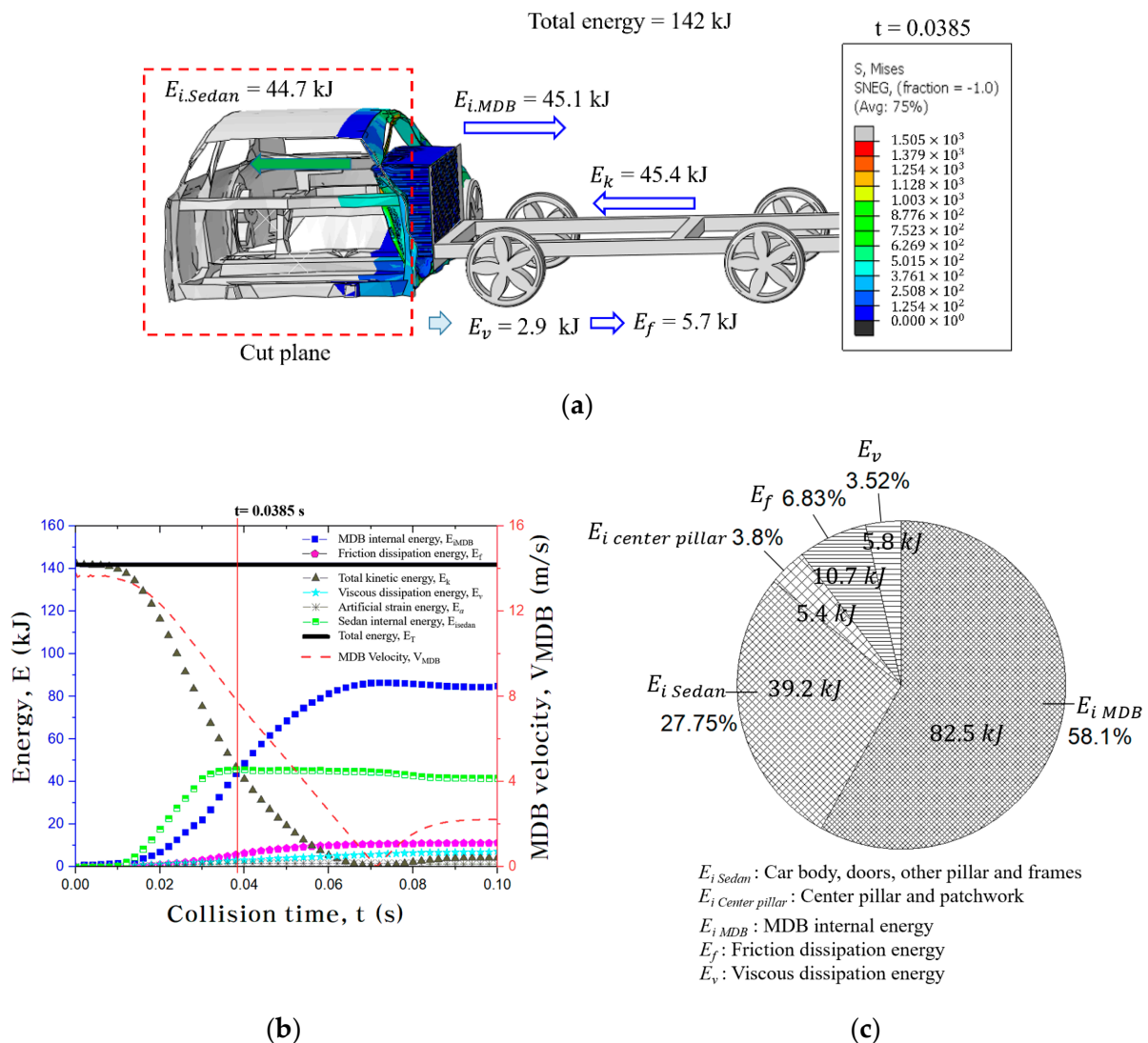


Figure 11. Energy conversion during side crash: (a) flow of energy distribution at $t = 0.0385$ s; (b) distribution of energies according to collision time; (c) distribution of energy conversion at $t = 0.071$ s.

Figure 11c shows the percentage of energy at $t = 0.071$ s, when MDB velocity was about 0 m/s. The E_{i-MDB} was 82.5 kJ, accounting 58.1% of the total energy, indicating that the 58.1% of total energy (142 kJ) was absorbed by the MDB during the side crash. On the other hand, the sum of $E_{i-Sedan}$ absorbed by the doors, automobile body, and other frames was 44.6 kJ, with 5.4 kJ of energy absorbed by the center pillar and PW. According to the above data, the center pillar and PW took 12% of the sedan internal energy. The inner part

of the center pillar was not included in this study. If the inner part of the center pillar been included, the center pillar, including the outer and inner portions, as well as the PW, would be expected to absorb 15~18% of the internal energy. The effect of PW and PS on energy distribution and intrusion resistance was investigated following, as reported below.

3.2.2. Effect of PW and PS on Elastic Strain Energy

Figure 12 shows the elastic strain energy (E_{es}) of the four kinds of center pillar (HPF, HPF + PW, HPF + PS, and HPF + PW + PS) during a side crash. For the HPF center pillar, the maximum E_{es} was 0.851 kJ at collision time (t) = 0.064 s and decreased to 0.30 kJ after the collision as a result of elastic recovery. When the PW was applied to the HPF center pillar, the maximum E_{es} increased to 0.928 kJ at t = 0.056 s. Because the rigidity of the HPF center pillar with PW increased, the absorption of elastic energy improved significantly. However, for the HPF center pillar with PS, the maximum E_{es} decreased to 0.655 kJ at t = 0.061 s. When the PS was applied to the bottom region of the HPF center pillar, because the stiffness of the HPF center pillar with PS decreased, the absorbed energy decreased in terms of elastic deformation.

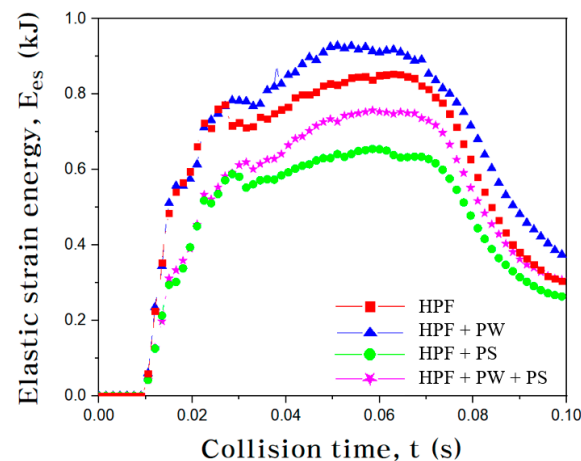


Figure 12. Elastic strain energy (E_{es}) of the four kinds of the center pillar during a side crash.

Figure 13 shows the maximum E_{es} of the four types of center pillar for detailed evaluation of energy absorption of PW and PS. The E_{es} of the HPF center pillar with PW was 0.1 kJ, accounting for 10% of the total energy absorbed by the HPF center pillar with PW. The E_{es} of the HPF center pillar with PS decreased to 0.655~0.660, regardless of the inclusion of PW.

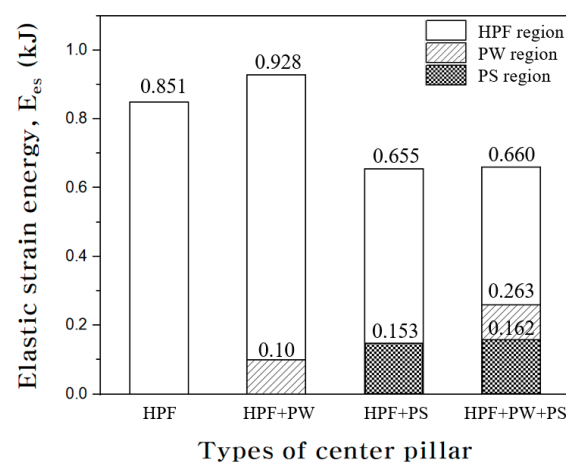


Figure 13. Maximum elastic strain energy (E_{es}) of the four types of center pillar.

3.2.3. Effect of PW and PS on Plastic Dissipated Energy

Figure 14 shows the plastic deformation energy (E_p) of the four kinds of the center pillar during a side crash. For the HPF center pillar, E_p increased to 4.538 kJ during deformation. The E_p was maintained after the collision, in contrast to the E_{es} , as a result of permanent deformation. For the HPF center pillar with PS, the E_p increased to 4.998 kJ at 0.1 s. The E_p of the HPF center pillar with PS was higher than that of the HPF center pillar. When PS was applied to the HPF center pillar, a large deformation occurred in the soft bottom region of the center pillar as a result of the ductility. As a result, the absorbed energy improved by 9.3%. However, there was no difference in absorbed energy between the HPF center pillar and the HPF center pillar with PW in terms of plastic deformation.

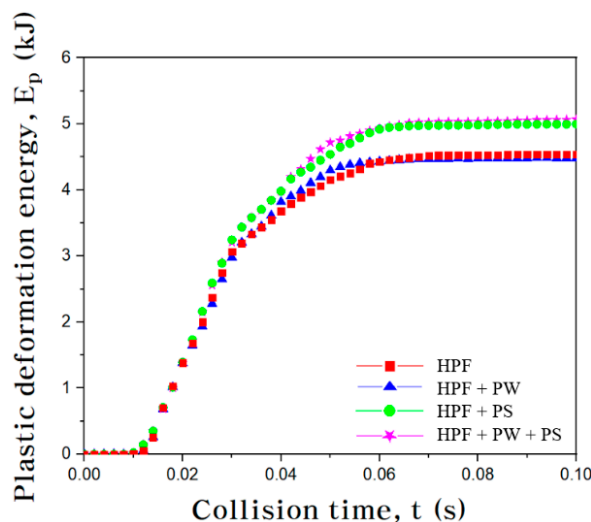


Figure 14. Plastic deformation energy (E_p) of the four kinds of the center pillar during side crash.

Figure 15 shows the maximum E_p of the four types of center pillar. For the HPF center pillar with PS and the HPF center pillar with PW and PS, 2.52~2.54 kJ of E_p was absorbed in the PS region, i.e., the bottom region of the center pillar. In terms of plastic deformation, the effect of PW was minimal, unlike elastic strain energy, whereas the E_p of the PS region accounted for 49.8~50.9% of the total plastic deformation energy between the HPF center pillar with PS and the HPF center pillar with PW and PS.

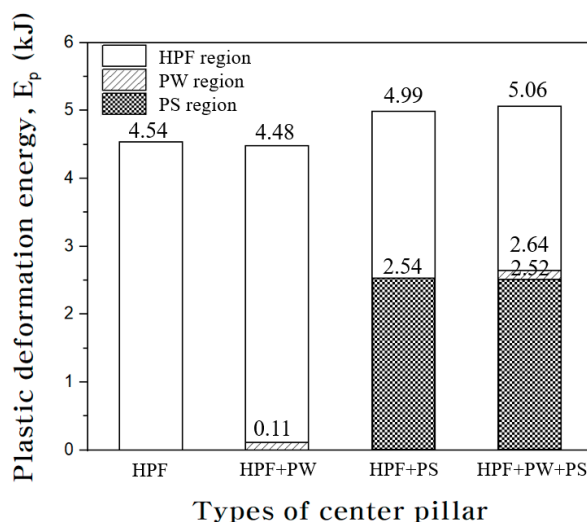


Figure 15. Maximum plastic deformation energy (E_p) of the four types of center pillar.

3.2.4. Effect of PW and PS on Internal Energy

Figure 16 shows the internal energy (E_i) of the four kinds of center pillar during a side crash. The total internal energy resulting from a collision consists of several energies and can be expressed by Equation (14):

$$E_i = E_{es} + E_p + E_a + E_{others} \quad (14)$$

where E_i is the internal energy; E_{es} is the elastic strain energy; E_p is the plastic deformation energy; E_a is the artificial strain energy; and E_{others} is the energy dissipated by creep, viscoelasticity, and swelling.

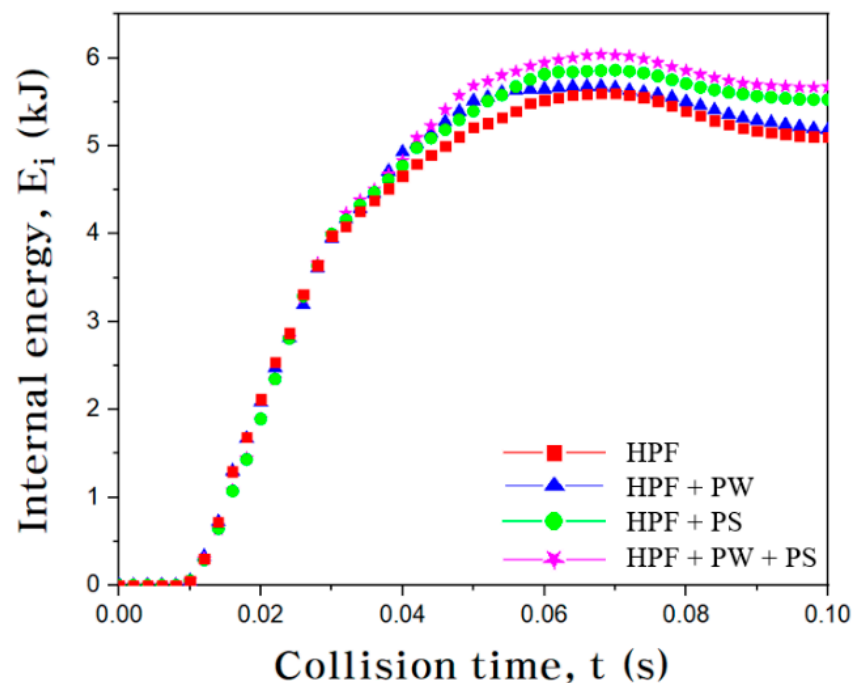


Figure 16. Internal energy (E_i) of the four kinds of center pillar during a side crash.

Generally, E_{es} and E_p are the dominant factors affecting E_i during a collision, and the contributions of other energies are relatively small. Therefore, in this study, the internal energy was expressed as the sum of E_{es} and E_p , excluding other types of energy, such as viscoelasticity, friction, and creep energy. In terms of internal energy, when the PS technique was applied to the HPF center pillar, there was a slight difference in the absorbed energy. However, a synergistic effect occurred when PW and PS were applied to the HPF center pillar, and a large amount of energy was absorbed, as shown in Figure 16.

Figure 17a shows the maximum E_i for the four types of center pillar. As shown in Figure 17a, there is almost no difference in the plastic deformation energy between the HPF center pillars with and without PW. The PW was welded on the upper part of the HPF center pillar to increase the stiffness, but the impact region was applied from the middle to the bottom, as shown in Figure 17b. Therefore, small deformation occurred in the PW. Likewise, a comparison between the HPF center pillar with PS and the HPF center pillar with PW and PS revealed similar phenomenon with respect to the absorbed plastic deformation energy. Based on the above results, it is necessary to review whether PS technology should be applied in light of the relationship between technical performance and manufacturing cost.

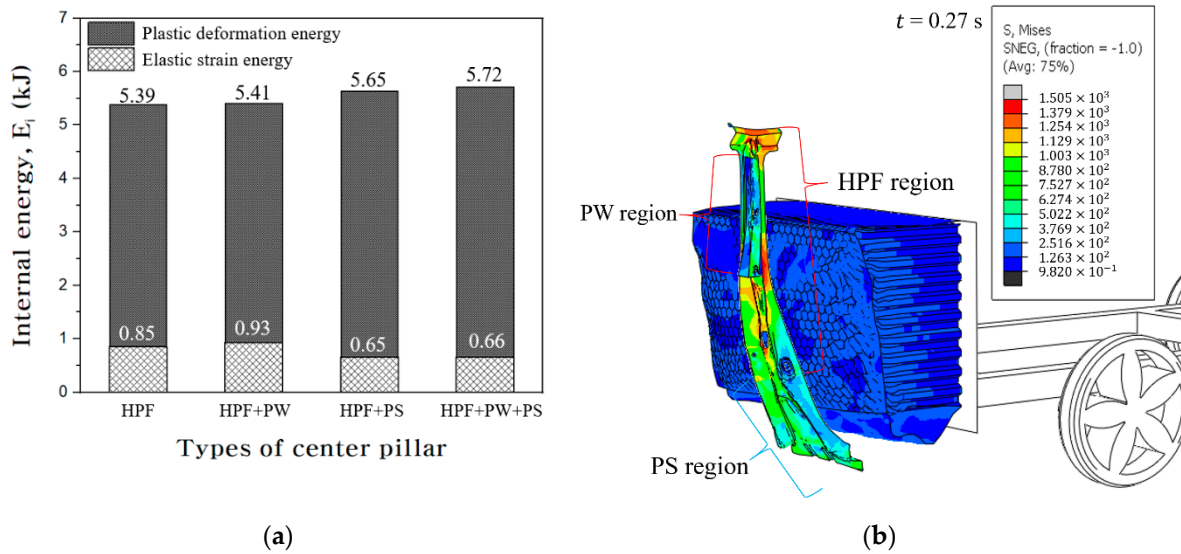


Figure 17. (a) Maximum internal energy (E_i) for the four types of center pillar. (b) Stress distribution of the center pillar during collision.

3.2.5. Effect of PW and PS on the Intrusion Resistance

During a side crash, a large amount of energy is absorbed. However, if the material is soft and a large amount of deformation occurs, the intrusion displacement increases, putting the passenger in danger. Therefore, it is important to evaluate intrusion displacement for passenger safety, as well as collision energy absorption.

As shown in Figure 18a, because both the center pillar and the MDB were deformed during the collision, the maximum intrusion displacement was calculated according to Equation (15).

$$d_{max.i} = d_{max.DMB}(t) - L_b \tag{15}$$

where $d_{max.DMB}$ is the maximum displacement of DBM, and L_b is the barrier length.

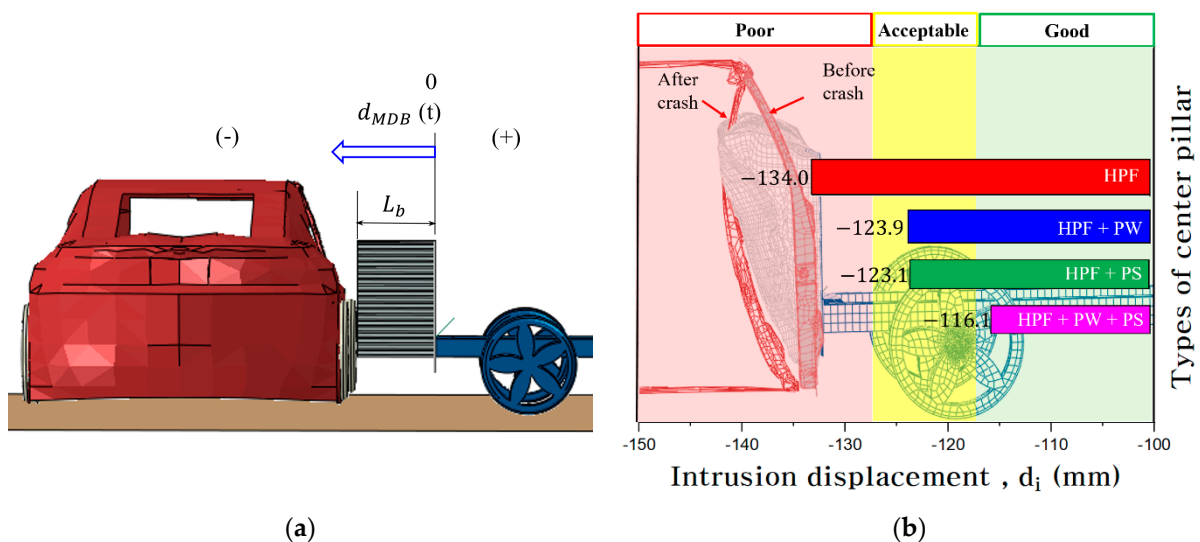


Figure 18. (a) Introduction of d_{MDB} and L_b . (b) Simulation data on intrusion displacement (d_i) of the four kinds of center pillar.

The evaluation method for the anti-intrusion resistance was introduced according to IIHS guidance. The primary performance of the center pillar is related to anti-intrusion resistance against side impact. According to the IIHS rating protocol, the center line of

the vehicle's seat was generally in compliance with standard of the measured intrusion displacement, as shown in Figure 18b, with categories of good, acceptable, marginal, and poor [25]. In this study, multistructures, such as automobile seats, dummies, and windows were, not considered, so the maximum intrusion of the HPF center pillar with PW was used as the acceptable distance, achieving an acceptable level. As shown in Figure 18b, the maximum intrusion displacement of the HPF center pillar and the HPF center pillar with PW were -134.0 mm and -123.9 mm, respectively. When the stiffness of the upper part was strengthened with PW, the safety of the intrusion displacement was also improved by 7.5%. Likewise, in the case of the HPF center pillar with PS, the maximum intrusion displacement was -123.1 mm. A similar result was achieved with the HPF center pillar with PW. On the other hand, the maximum intrusion displacement of the HPF center pillar with PW and PS was -116.1 mm, representing an improvement of 13.4%. When the PW and PS were combined, a synergistic effect occurred.

4. Conclusions

In the side crash simulation performed in the present study, the effects of the HPF center pillar with PW and PS on energy distribution and anti-intrusion resistance were investigated, and the following conclusions were obtained:

1. During a side crash collision, the effect of PW in the HPF center pillar on plastic deformation energy was minimal but important with respect to elastic strain energy and intrusion resistance. When PW was applied to the HPF center pillar to strengthen the stiffness, the elastic strain energy and intrusion displacement were 10.0 and 7.5% respectively.
2. Because the PS technique provided ductility to the lower region of the HPF center pillar, large deformation occurred, and the plastic deformation energy was improved significantly by 10%. The plastic deformation energy of the PS region accounted for 49.8~50.9% of the plastic deformation energy of the HPF center pillar with PS.
3. In terms of total internal energy, the PS technique achieved better results than the PW technique. The maximum intrusion displacement of the HPF center pillar with PS was similar to that of the HPF center pillar with PW. In the case of the HPF center pillar with PW and PS, the maximum intrusion displacement was improved by 13.4%, and a synergistic effect of PW and PS occurred.

Author Contributions: Methodology, M.S.L.; writing—original draft, M.S.L.; writing—review and editing, M.S.L., C.K.J., and J.S.; software, M.S.L.; formal analysis, M.S.L.; investigation, O.D.L. and T.L.; funding, J.S.; validation and supervision: C.K.J. All authors have read and agreed to the published version of the manuscript.

Funding: This research was supported by the Ministry of Trade, Industry & Energy (20017450). This work was supported by the Energy technology development program (20206310200010, Advanced Remanufacturing of industrial machinery based on domestic CNC and building infrastructure for remanufacturing industry) funded By the Ministry of Trade, Industry & Energy (MOTIE, Korea).

Data Availability Statement: All datasets associated with this research are available upon request to the corresponding author.

Conflicts of Interest: The authors declare no conflict of interest.

References

1. Frómeta, D.; Lara, A.; Molas, S.; Casellas, D.; Rehr, J.; Suppan, C.; Larour, P.; Calvo, J. On the correlation between fracture toughness and crash resistance of advanced high strength steels. *Eng. Fract. Mech.* **2019**, *205*, 319–332. [[CrossRef](#)]
2. Ma, B.L.; Wan, M.; Li, X.J.; Wu, X.D.; Diao, S.K. Evaluation of limit strain and temperature history in hot stamping of advanced high strength steels (AHSS). *Int. J. Mech. Sci.* **2017**, *128–129*, 607–613. [[CrossRef](#)]
3. Ashok, K.P.; Merbin, J.; Udaya, B.K.; Pradeep, L.M. Advanced High-Strength Steels for Automotive Applications: Arc and Laser Welding Process, Properties, and Challenges. *Metals* **2022**, *12*, 1051.
4. Christian, L.; Norbert, K.; Frank, B.K. Advanced High Strength Steels (AHSS) for Automotive Applications—Tailored Properties by Smart Microstructural Adjustments. *Steel Res. Int.* **2017**, *88*, 1700210.

5. Park, J.Y.; Jo, M.C.; Song, T.J.; Kim, H.S.; Sohn, S.S.; Lee, S.K. Ultra-high strength and excellent ductility in multi-layer steel sheet of austenitic hadfield and martensitic hot-press-forming steels. *Mater. Sci. Eng. A*. **2019**, *759*, 320–328. [[CrossRef](#)]
6. Kim, H.G.; Won, C.H.; Choi, S.G.; Gong, M.G.; Park, J.G.; Lee, H.J.; Yoo, J.H. Thermo-Mechanical Coupled Analysis of Hot Press Forming with 22MnB5 Steel. *Int. J. Automot. Technol.* **2019**, *20*, 813–825. [[CrossRef](#)]
7. Lee, M.S.; Moon, Y.H. Collision resistance of a lightweight center pillar made of AA7075-T6. *Int. J. Automot. Technol.* **2019**, *22*, 853–862. [[CrossRef](#)]
8. Liu, Y.; Zhu, Z.; Wang, Z.; Zhu, B.; Wang, Y.; Zhang, Y. Formability and lubrication of a B-pillar in hot stamping with 6061 and 7075 aluminum alloy sheets. *Procedia Eng.* **2017**, *207*, 723–728. [[CrossRef](#)]
9. Lee, M.S.; Seo, H.Y.; Kang, C.G. Comparative study on mechanical properties of CR340/CFRP composites through three point bending test by using theoretical and experimental methods. *Int. J. Precis. Eng. Manufac. Green Technol.* **2016**, *3*, 359–365. [[CrossRef](#)]
10. Çavuşoğlu, O.; Çavuşoğlu, O.; Yılmazoğlu, A.G.; Üzel, U.; Aydın, H.; Güral, A. Microstructural features and mechanical properties of 22MnB5 hot stamping steel in different heat treatment conditions. *J. Mater. Res. Tech.* **2020**, *9*, 10901–10908.
11. Omer, K.; Kortenaar, L.T.; Butcher, C.; Worswick, M.; Malcolm, S.; Detwiler, S. Testing of a hot stamped axial crush member with tailored properties—Experiments and models. *Int. J. Impact Eng.* **2017**, *103*, 12–28. [[CrossRef](#)]
12. Shi, D.Y.; Watanabe, K.; Naito, J.; Funada, K.; Yasui, K. Design optimization and application of hot-stamped B pillar with local patchwork blanks. *Thin Walled Struct.* **2022**, *170*, 108523. [[CrossRef](#)]
13. Mori, K.I.; Kaido, T.; Suzuki, Y.; Nakagawa, Y.; Abe, Y. Combined process of hot stamping and mechanical joining for producing ultra-high strength steel patchwork components. *J. Manuf. Process.* **2020**, *59*, 444–455. [[CrossRef](#)]
14. Ahmad, M.A.; Zakaria, A. Optimization of Spot Welds on Patchwork Blank for Hot Forming Process. *Appl. Mech. Mater.* **2014**, *606*, 177–180. [[CrossRef](#)]
15. Chengxi, L.; Zhongwen, X.; Weili, X. Hot stamping of patchwork blanks: Modelling and experimental investigation. *Int. J. Adv. Manuf. Technol.* **2017**, *92*, 2609–2617.
16. Gao, T.H.; Ying, L.; Dai, M.; Shen, G.; Hu, P.; Shen, L. A comparative study of temperature-dependent interfacial heat transfer coefficient prediction methods for 22MnB5 steel in spray quenching process. *Int. J. Therm. Sci.* **2019**, *139*, 36–60. [[CrossRef](#)]
17. Ota, E.; Yogo, Y.; Iwata, N. CAE-based process design for improving formability in hot stamping with partial cooling. *J. Mater. Process Technol.* **2019**, *263*, 198–206. [[CrossRef](#)]
18. Bok, H.H.; Choi, J.W.; Suh, D.W. Stress development and shape change during press-hardening process using phase-transformation-based finite element analysis. *Int. J. Plast.* **2015**, *73*, 142–170. [[CrossRef](#)]
19. Kim, D.K.; Woo, Y.Y.; Park, K.S. Advanced induction heating system for hot stamping. *Int. J. Adv. Manufac. Technol.* **2018**, *99*, 583–593. [[CrossRef](#)]
20. Lee, M.S.; Lim, O.D.; Kang, C.G.; Moon, Y.H. Combined application of patchwork and partial softening to enhance the collision resistance of the center pillar. *Int. J. Crashworthiness* **2022**, *27*, 688–699. [[CrossRef](#)]
21. IMATEC. Available online: <https://www.imatec.it/> (accessed on 11 May 2021).
22. Yin, H.; Xiao, Y.; Wen, G. Multiobjective Optimisation for Foam-Filled Multi-Cell Thin-Walled Structures Under Lateral Impact. *Thin Walled Struct.* **2015**, *94*, 1–12. [[CrossRef](#)]
23. Abaqus User's Manual 6.11. 2010. Available online: http://130.149.89.49:2080/v6.11/pdf_books/CAE.pdf (accessed on 11 May 2021).
24. Ciulia, V.; Sterfania, B.; Andrea, G.; Xiao, C. Numerical modeling of the 22MnB5 formability at high temperature. *Procedia Manuf.* **2019**, *29*, 428–434.
25. Young, J. *Side Impact Crashworthiness Evaluation; Crash Test Protocol Ver. IX User Guide*; Insurance Institute for Highway Safety (IIHS): Arlington, VA, USA, 2016.